Journal of Biomedical Optics

BiomedicalOptics.SPIEDigitalLibrary.org

Rapid, noninvasive quantitation of skin disease in systemic sclerosis using optical coherence elastography

Yong Du
Chih-Hao Liu
Ling Lei
Manmohan Singh
Jiasong Li
M. John Hicks
Kirill V. Larin
Chandra Mohan

SPIE.

Yong Du, Chih-Hao Liu, Ling Lei, Manmohan Singh, Jiasong Li, M. John Hicks, Kirill V. Larin, Chandra Mohan, "Rapid, noninvasive quantitation of skin disease in systemic sclerosis using optical coherence elastography," *J. Biomed. Opt.* **21**(4), 046002 (2016), doi: 10.1117/1.JBO.21.4.046002.

Rapid, noninvasive quantitation of skin disease in systemic sclerosis using optical coherence elastography

Yong Du,[a,†] Chih-Hao Liu,[a,†] Ling Lei,[a] Manmohan Singh,[a] Jiasong Li,[a] M. John Hicks,[b] Kirill V. Larin,[a,c,d,*] and Chandra Mohan[a,*]
[a]University of Houston, Department of Biomedical Engineering, 3605 Cullen Boulevard, Houston, Texas 77204, United States
[b]Texas Children's Hospital, Pathology & Immunology and Pediatrics, Baylor College of Medicine, 6621 Fannin Street, Houston, Texas 77030, United States
[c]Baylor College of Medicine, Molecular Physiology and Biophysics, One Baylor Plaza, Houston, Texas 77030, United States
[d]Samara State Aerospace University, Department of Laser and Biotechnical Systems, 34 Moskovskoye shosse, Samara 443086, Russia

Abstract. Systemic sclerosis (SSc) is a connective tissue disease that results in excessive accumulation of collagen in the skin and internal organs. Overall, SSc has a rare morbidity (276 cases per million adults in the United States), but has a 10-year survival rate of 55%. Currently, the modified Rodnan skin score (mRSS) is assessed by palpation on 17 sites on the body. However, the mRSS assessed score is subjective and may be influenced by the experience of the rheumatologists. In addition, the inherent elasticity of skin may bias the mRSS assessment in the early stage of SSc, such as oedematous. Optical coherence elastography (OCE) is a rapidly emerging technique, which can assess mechanical contrast in tissues with micrometer spatial resolution. In this work, the OCE technique is applied to assess the mechanical properties of skin in both control and bleomycin (BLM) induced SSc-like disease noninvasively. Young's modulus of the BLM-SSc skin was found be significantly higher than that of normal skin, in both the *in vivo* and *in vitro* studies ($p < 0.05$). Thus, OCE is able to differentiate healthy and fibrotic skin using mechanical contrast. It is a promising new technology for quantifying skin involvement in SSc in a rapid, unbiased, and noninvasive manner. © *2016 Society of Photo-Optical Instrumentation Engineers (SPIE)* [DOI: 10.1117/1.JBO.21.4.046002]

Keywords: scleroderma; elasticity; optical coherence elastography; elastic wave velocity; dermatology.

Paper 150682RR received Oct. 13, 2015; accepted for publication Mar. 7, 2016; published online Apr. 5, 2016.

1 Introduction

Systemic sclerosis (SSc) is a connective tissue disease that results in excessive accumulation of collagen in the skin and internal organs.[1,2] Since increased fibrosis underlies the common presentation of SSc, current diagnostic approaches in SSc focus on assessing the degree of fibrosis. Previous work has estimated the prevalence of SSc in the United States to be ~276 cases per million adults and with 19.3 new cases per million adults each year.[3] Although SSc is a rare disorder, Mayes et al. reported that the survival rate was 77.9% at 5 years, but dropped to 55.5% at 10 years after diagnosis. The median survival after diagnosis was ~11 years. This finding suggests that SSc has high case-specific mortality, as more than half of SSc patients will eventually die as a direct result of the disease. In addition to its high mortality, the disease also significantly reduces the function and quality of life of SSc patients.[4,5] Considering the high case-specific mortality and morbidity, early diagnosis is critical in SSc management and treatment.[6]

Traditionally, the modified Rodnan skin score (mRSS) system, a measure of skin thickness, is widely used to measure the skin involvement in SSc patients. The degree of the score is determined manually pinching skin at 17 sites on the body.[7] For each area, a score is given based on the palpation, and the individual values are summed to get the total skin score. The assessment of the mRSS score can be time consuming and is heavily dependent on the palpation experience of rheumatologist, which results in a subjective observation that may cause inter- and intra-observer variabilities.[8,9] Furthermore, the skin elasticity may bias the palpation test for detecting SSc in its early oedematous stages.[10] A diseased patient may be scored as 0, but have thickened skin due to its reduced stiffness due to oedematous. Therefore, a quantitative, rapid, and objective diagnostic approach for SSc is still needed to facilitate early disease detection.[11]

Several imaging modalities have been used to characterize fibrosis skin, including ultrasound imaging (USI) and optical coherence tomography (OCT). However, all imaging techniques have an inherent trade-off between spatial resolution and penetration depth.[12,13] High-frequency ultrasound has sufficient penetration depth (~15 mm) for an accurate measurement of skin thickness,[14] but insufficient spatial resolution (~300 μm) to characterize micrometer scale features.[15] The echogenicity,[10] tissue attenuation, and backscattering properties[16] have been suggested as metrics for SSc assessment. In contrast, OCT can provide micrometer scale spatial resolution ($\leq$10 μm) with an imaging depth of a few millimeters in scattering media such as skin.[17,18] Abignano et al. initially demonstrated the correlation among OCT structural images, histology, and mRSS.[1] The pathological evidence during SSc progression can be observed

*Address all correspondence to: Kirill V. Larin, E-mail: klarin@uh.edu; Chandra Mohan, E-mail: cmohan@uh.edu

†Equal contribution as cofirst authors

1083-3668/2016/$25.00 © 2016 SPIE

from the dermal–epidermal junction in OCT images, thus highlighting the promising application of OCT to monitor SSc progression.[1] Although there is a paucity of research using OCT to study SSc,[13] polarization-sensitive OCT has been utilized to detect the collagen distribution in epidermis and dermis layers, especially the dermal–epidermal junction,[19,20] which would be useful for monitoring dermal thickening during SSc onset. Compared with USI, OCT has superior spatial resolution and sufficient penetration depth to image the subcutaneous fat in human skin,[21] demonstrating its capability to detect the pathological changes in the dermal layers. Furthermore, tissue properties can be quantitatively assessed for various optical parameters based on the OCT signal, such as optical attenuation and speckle variance.[22] Although OCT optical properties can reflect changes in the tissue due to a disease, the biomechanical properties of tissue can provide an alternative form of contrast for disease detection and diagnostics. In the case of SSc, it is well understood that the mechanical properties of skin change significantly due to collagen thickening and, thus, may provide a powerful basis for disease detection and staging.[23]

Previously, contact-based mechanical testing devices, such as the Durometer[24] and Vesmeter,[25] have been, respectively, utilized to assess the hardness and mechanical properties of skin. However, with the earlier approaches, subjective bias and mechanical damage after repeated testing can reduce disease detection accuracy. OCT-based elastography, which is termed optical coherence elastography (OCE), is a rapidly emerging technique, which can assess mechanical contrast in tissues with micrometer spatial resolution.[26,27] In this work, we demonstrate the power of OCE technology for noncontact evaluation of skin from normal mice as well as mice induced to have SSc-like disease using bleomycin (BLM-SSc). A phase-stabilized swept source optical coherence elastography (PhS-SSOCE) system was used to image the propagation of a focused air-pulse induced elastic wave, and the Young's modulus was quantified from the elastic wave group velocity. OCE measurements were taken at the center and boundary of the diseased region to determine whether OCE can detect SSc at regions with less severe disease progression. The results demonstrate that OCE was able to accurately detect fibrotic skin, even at the periphery of the diseased region. To validate this approach, the hydroxyproline content, semiquantitative histological analysis, and the skin thickness were also assessed, in parallel. The OCE readouts and hydroxyproline content, histology, and thickness results were in good agreement, demonstrating that OCE is a promising and potentially useful tool for quantifying skin involvement in SSc in a rapid, unbiased, and noninvasive manner.

2 Materials and Methods

2.1 *Sample Preparation*

Eight-week-old, pathogen-free, female C3H/HeJ mice were purchased from Jackson Laboratory (Bar Harbor), and pharmacologic grade BLM was obtained from Teva Parenteral Medicines Inc. (Irvine, California). BLM was dissolved in sterile phosphate buffered saline (PBS) at a concentration of 1 mg/mL and was intradermally administered to shaved lower dorsal skin once per day in a total volume at 100 μL/day, for four weeks. The shaved area is almost the same among all the mice. Since the BLM powder was dissolved in PBS for the diseased group, we gave the control group 100 μL sterile PBS each day to remove inter-treatment variability due to the injection itself. The day following the final PBS or BLM treatment, all mice were subjected to either *in vivo* or *in vitro* skin OCE examination. After the OCE assessment, skin tissue from both *in vivo* and *in vitro* mice was collected for the further histological analysis. All studies and procedures were approved by the Animal Care and Use Committee of University of Houston. The sample information has been listed in Table 1.

Table 1 Sample size for histological analyses.

Skin condition	Histological study
Healthy	18
SSc	13

2.2 *Histological Analyses*

Skin tissue was fixed in 10% formalin solution and embedded in paraffin. The paraffin sections were stained with hematoxylin and eosin (H&E) to evaluate histopathological changes and with Masson stain to detect collagen fibers in tissues. Dermal thickness, which was defined as the thickness of the skin from the top of the granular layer to the junction between the dermis and subcutaneous fat, was measured after taking photographs. Histological changes were assessed by a pathologist in a blinded manner. A semiquantitative scale was used to score dermal inflammation and skin fibrosis (0 none, 1 mild, 2 moderate, 3 severe). For each sample, at least four points have been randomly selected to measure the thickness, and the final thickness of each sample is the average of these four measurements.

2.3 *Skin Hydroxyproline Content Measurement*

A hydroxyproline assay kit was purchased from Sigma-Aldrich (MAK008-1KT, St. Louis). Hydroxyproline is a modified amino acid unique to collagen. Hence, fibrosis can be quantitatively estimated by determining the total hydroxyproline content of the tissue. Briefly, skin tissue was first homogenized and hydrolyzed with 12 M hydrochloric acid 120°C for 3 h. The supernatant was then collected to determine the hydroxyproline concentration by the reaction of oxidized hydroxyproline with 4-(Dimethylamino) benzaldehyde. The results were expressed as micrograms of hydroxyproline per gram of skin.

2.4 *Optical Coherence Elastography Experimental Procedure*

Two separate OCE measurements were performed: *in vitro* assessment of murine dorsal skin samples and *in vivo* assessment on anesthetized mice. During the *in vivo* measurements, all mice ($N = 17$) were anesthetized with isoflurane, and *in vivo* OCE measurements were performed on the central versus the peripheral regions of the diseased skin on the lower back in order to assess the feasibility of detecting SSc at the periphery of the diseased region. The dorsal spine was beneath the center region, but not imaged in the peripheral region. The *in vitro* measurements were taken at the peripheral of the diseased spots on the dorsal skin samples, obtained after euthanizing the mice ($N = 14$). All *in vitro* experiments were completed within 12 h after the skin samples were harvested. A summary of how the samples were used for OCE experiment is listed in Table 2.

Table 2 Samples used for OCE assessment *in vivo* ($N = 17$) and *in vitro* ($N = 14$).

	OCE measurement position			
	Center region		Peripheral region	
Sample condition	Healthy	SSc	Healthy	SSc
In vivo	4	4	5	4
In vitro	0	0	9	5

2.5 *Phase-Stabilized Swept Source Optical Coherence Elastography System*

A home-built PhS-SSOCE system is composed of a phase-stabilized swept source optical coherence tomography (PhS-SSOCT) system and a focused air-pulse delivery device, as shown in Fig. 1. The PhS-SSOCT system utilized a broadband swept laser source (HSL2000, Santec Inc.) with a central wavelength of $\sim 1310 \pm 75$ nm and A-scan rate of 30 kHz. A fiber Bragg grating was utilized for A-scan triggering and phase stabilization. The axial resolution of the system was ~ 11 μm (z-axis) in air, and the phase stability of the system was experimentally measured as ~ 16 mrad, which corresponds to the detectable displacement of ~ 3 nm.[28] The corresponding sensitivity of this system was 104 dB. Further details of the PhS-SSOCT system can be found in our previous work.[28,29] The PhS-SSOCT system was synchronized with a pulse generator that drove an electronically controlled pneumatic solenoid. The focused air-pulse was expelled through the solenoid and out of a cannula port with a flat edge and inner diameter of ~ 150 μm. The air source pressure was controlled by a standard pneumatic valve and was monitored with an air pressure gauge. The air port tip was aligned with the OCE imaging plane from the OCT structural image, as seen by the shadow below the air port tip in Fig. 2(a). Based on this alignment, the largest displacement position can be observed and determined as the first position for the elastic wave group velocity computation. The force of the focused air-pulse on the mouse skin was ~ 2 Pa,[30] and the localized air-pulse was precisely positioned by a three-dimensional (3-D) linear micrometer stage. Successive 501 M-mode images (M-B mode) were acquired in an ~ 6 mm line where the excitation was at the center of the scan range as shown in Fig. 2(a). Because the elastic wave propagation distance in the skin was limited to ~ 1 mm, center excitation allowed for effectively taking measurements from both sides of the excitation. The lateral resolution was ~ 12 μm. Each M-mode image was recorded for 3000 A-lines (100 ms) to monitor the wave propagation as shown in Fig. 2(c). The displacement images were reconstructed from the displacement profiles at all the imaged positions to visualize the elastic wave propagation at the effective frame rate of 30 kHz. In the reconstructed movie, a five-pixel moving-averaging window was performed in both spatial and temporal domains. By synchronizing the air-pulse with the M-mode frame trigger, the PhS-SSOCT system effectively imaged the elastic wave propagation and the OCT images can be reconstructed from the recorded A-lines.[31]

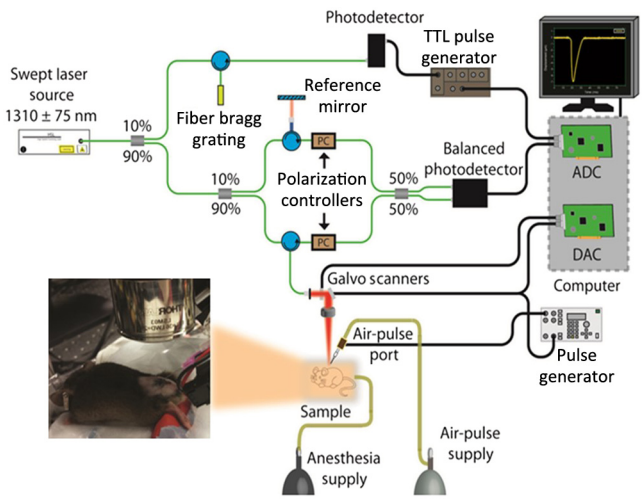

Fig. 1 Schematic of the PhS-SSOCE experimental setup that was used for studying BLM-induced SSc skin and healthy skin specimens.

2.6 *Elastic Group Wave Velocity Calculations*

Figure 2(a) shows a 3-D OCT structural image of a healthy skin sample with the OCE measurement region and excitation position. Figure 2(b) shows a two-dimensional (2-D) structural OCT image (B-scan) corresponding to the OCE measurement region. The stripe artifacts seen in the structural image are due to the respiration of the mouse. Figure 2(c) illustrates selected typical elastic wave vertical temporal displacement profiles at OCE measurement positions corresponding to the marked positions in Fig. 2(b).

The vertical temporal displacement profiles of the elastic wave at the surface, $d_{\text{surface}}(t)$, were calculated from the raw unwrapped surface phase profiles, $\varphi_{\text{surface}}(t)$, using the following equation:[32]

$$d_{\text{surface}}(t) = \frac{\lambda_0}{2\pi n_{\text{air}}} \times \varphi_{\text{surface}}(t), \tag{1}$$

and the displacement profiles within the skin, $d_{\text{inside}}(t)$, were corrected due to the surface motion and refractive index mismatch between air and the tissue from the raw unwrapped phase profiles inside the skin, $\varphi_{\text{inside}}(t)$, using the following equation:[33]

$$d_{\text{inside}}(t) = \frac{\lambda_0}{2\pi n_{\text{skin}}} \times \left[\varphi_{\text{inside}}(t) + \varphi_{\text{surface}}(t) \times \frac{n_{\text{skin}} - n_{\text{air}}}{n_{\text{air}}}\right], \tag{2}$$

where λ_0 is the central wavelength of the laser source, and $n_{\text{skin}} = 1.4$ was the refractive index of the skin.[34] The time delay, Δt, of the elastic wave to propagate from a reference position near the excitation position to each of the OCE measurement position distance was determined by cross-correlation analysis of the normalized temporal displacement profiles. The elastic wave group velocity, c_g, for a given imaged in-depth layer was computed by a least squares linear fit of the propagation time delays to the corresponding OCE measurement positions.[35] The depth-wise median velocity was used as the elastic wave group velocity for that given sample to calculate the elasticity. The elastic wave was considered as a Rayleigh wave due to the geometry of the sample and boundary conditions.[36] Young's modulus was quantified from the group velocity, c_g, using[37]

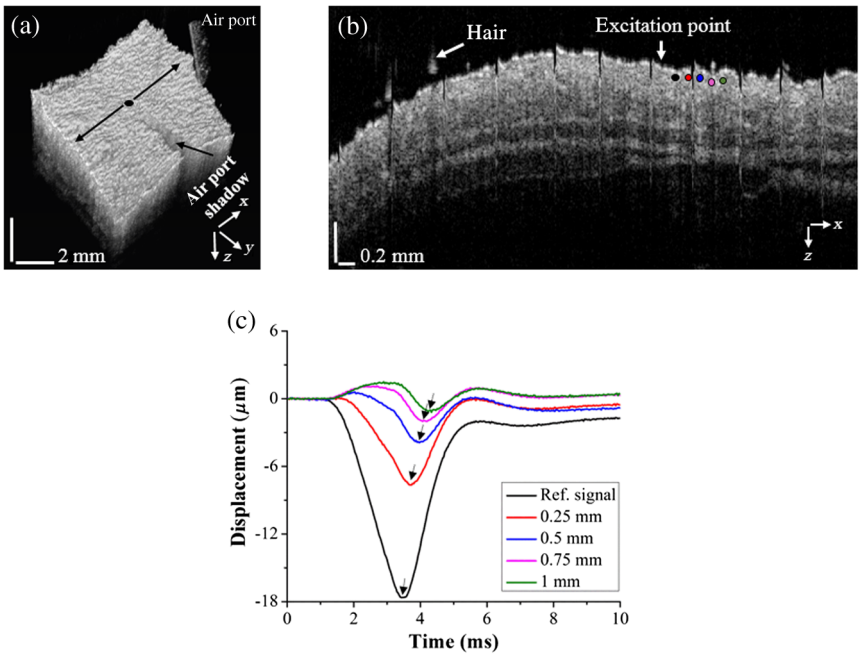

Fig. 2 The air port tip was aligned with the OCE imaging plane from the OCT structural image: (a) 3-D OCT structural image from a typical healthy skin sample. The OCE measurement region is marked by the black arrows and the excitation position is marked by the black dot in the middle. (b) 2-D OCT image corresponding to black arrows in (a) with the OCE measurement positions being indicated by the colored solid dots. (c) Selected temporal vertical displacement profiles of the healthy skin sample, measured from the corresponding positions marked in (b) with matching colored solid dots. The black arrows in (c) indicate the temporal delay during the wave propagation.

$$E = \frac{2\rho(1+v)^3}{(0.87+1.12v)^2} c_g^2, \tag{3}$$

where $\rho = 1100\ \mathrm{kg/m^3}$ is the density of the tissue and $\nu = 0.47$ is the Poisson's ratio.[38]

The computational window was ~1 mm (90 pixels) along the skin surface and 0.2 mm (50 pixels) in depth. To avoid specular reflections from the skin surface and subsequent saturation artifacts, the computational window was shifted beneath the surface by 50 μm (10 pixels). Because the elastic wave propagation was imaged in two directions, the Young's modulus was averaged from both directions and used as the single value for a given sample.

2.7 *Statistical Analysis*

Results were expressed as inter-sample means ± standard deviation. Statistical analysis was performed using GraphPad Software (California). Significance was determined using a two-tailed t test, and a p value <0.05 was considered significant.

3 Results

3.1 *Histopathology*

After four weeks of BLM injection, the histological changes around the injection sites were examined. We documented the presence of sclerotic skin with thickened collagen bundles and homogeneous deposition as determined by Masson's trichrome and H&E staining, as shown in Figs. 3(a)–3(d). The skin thickness in the BLM-SSc group (363 ± 25.94 μm) was significantly greater ($p < 0.001$) than the PBS control mice (203.6 ± 10.32 μm), as illustrated in Fig. 3(e). The skin fibrosis score and the skin hydroxyproline content of the BLM-SSc group was significantly higher ($p < 0.001$) than that of the PBS control group, as plotted in Figs. 3(f)–3(g). In addition, cellular infiltrates and a decrease in the amount of subcutaneous fat tissue were observed in the BLM treated mice, as illustrated in Figs. 3(b) and 3(d).

3.2 *Optical Coherence Tomography/Optical Coherence Elastography Assessment of Skin*

The epidermal–dermal junction (EDJ) is an easily identifiable structure that is clearly altered during SSc development[1] as seen in Fig. 4. From the OCT images in Fig. 4, the EDJ can be clearly seen in the healthy skin, while there is no clear demarcation in the SSc skin between the epidermis (E) and dermis (D). Moreover, additional structure in the dermis region cannot be seen in the SSc skin due to the more rapid light attenuation as a function of depth caused by collagen thickening. These features show promise for the use of OCT to detect SSc development by monitoring structural changes.

To investigate the biomechanical properties of the skin, a focused air-pulse induced a small amplitude (μm scale) deformation, which then propagated as an elastic wave. From Fig. 2(c), the elastic wave propagation and amplitude attenuation with increasing distance from the stimulation point are clearly evident in the healthy skin sample that was used. When OCE assessment was applied to the BLM-SSc skin, interesting differences were observed.

The elastic wave propagation profiles from the healthy skin (Video 1, top) and the BLM-SSc skin (Video 1, bottom) were significantly different after excitation. In Fig. 5(a), the

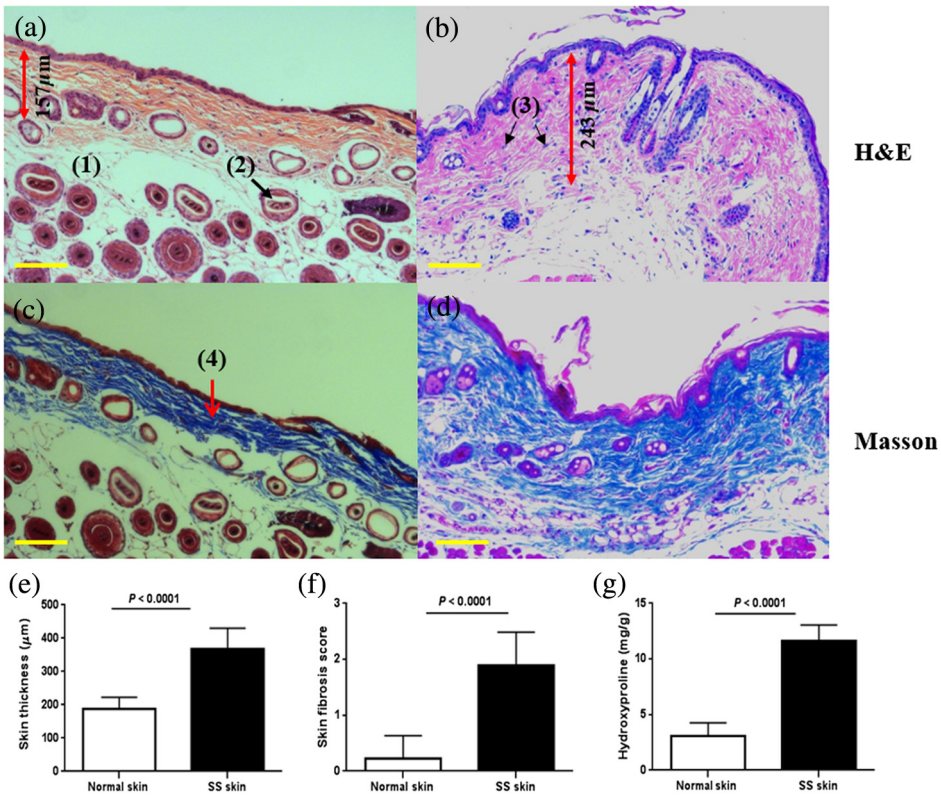

Fig. 3 Histopathological features of BLM-induced skin fibrosis. Representative H&E stained skin sections from (a) PBS-injected control group specimen and (b) BLM-injected skin sample, at 100× magnification. Compared to the PBS control group in (a), BLM-injected mice showed increased skin thickness, loss of subcutaneous fat tissue, as well as increased cellular infiltration. Representative sections stained with Masson's trichrome at 100× magnification from a (c) PBS-injected control group skin specimen and (d) BLM-treated sample. Thickened collagen bundles were observed in the BLM-injected mice, compared to the PBS-injected control mice. The scale bars represent the spatial distance of 100 μm. The main features of the skin have been shown in (a) to (d), including fat tissue (1), hair follicles (2), inflammatory cells (3), and collagen (4). The skin thickness measurement is also shown in (a) and (b) by the double-headed red arrow; (e) skin thickness, (f) skin fibrosis score, and (g) skin hydroxyproline content were significantly higher in the BLM-SSc mice than in the control mice. Shown data are representative of similar findings from 18 mice from the control group and 13 mice from the BLM-SSc group.

displacement amplitude decreased as the wave propagated through the sample is represented by the color scale from -1.5 to 1.5 μm to enable visualization of the elastic wave beyond 1 mm from the excitation. A displacement amplitude between -1.5 and 1.5 μm is represented as a color gradient changing from blue to red, as shown in Figs. 5(b)–5(f). Put simply, downward displacements < -1.5 μm are represented by full blue color, and upward displacements >1.5 μm are shown in full red. The alternative changes of colors reveal the propagation pattern of the elastic wave in the skin. From Figs. 5(b)–5(d), it can be seen that the elastic wave propagates further in the BLM-SSc skin as compared to the healthy skin after excitation. The blue color appearing near the excitation in Figs. 5(e) and 5(f) is due to the slow recovery of the skin displacement caused by the excessive excitation force. Interestingly, during the elastic wave propagation in skin, there were no significant changes in amplitude of the wave displacements (axial direction), which may be due to several factors such as the relatively long wavelength of the wave (few mm) in relation to the effective imaging depth (<1.3 mm). The comparison between the elasticity of healthy skin and central region of the diseased BLM-SSc skin as measured during the *in vivo* OCE experiments is plotted in

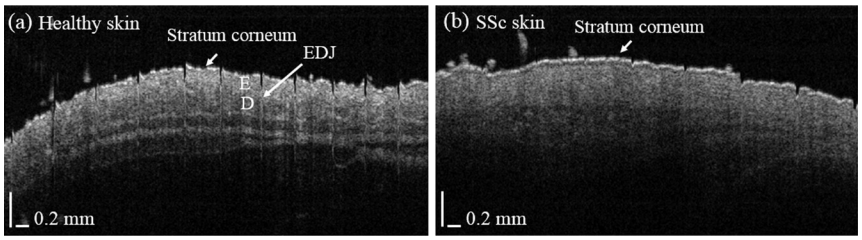

Fig. 4 Typical OCT images of the healthy and SSc skin. The EDJ can be clearly identified in the healthy skin, as well the epidermis (E), and dermis (D) layers.

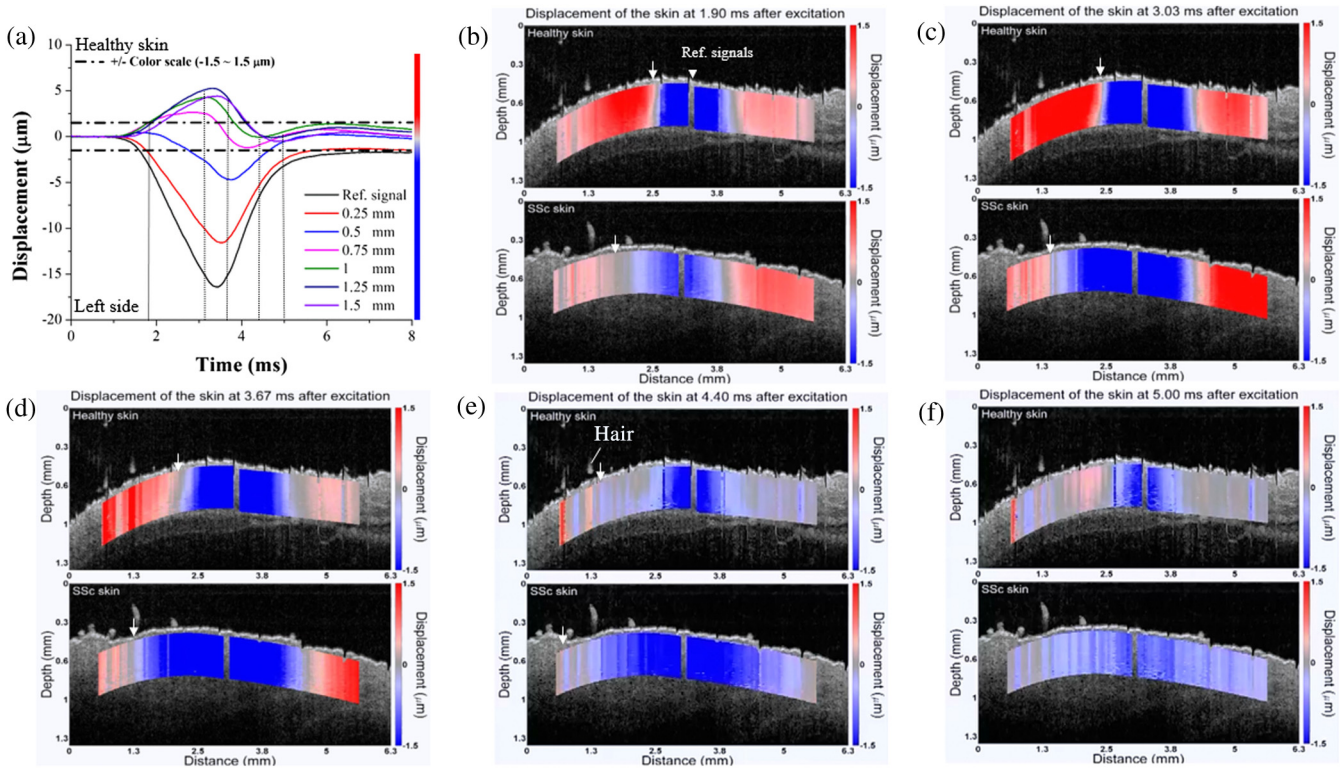

Fig. 5 Elastic wave propagation in the skin, as assessed by OCE. The displacement profiles of the healthy skin with color scale are plotted in (a). Depicted are the propagation profiles (Video 1) of the elastic wave in a typical healthy (top) and SSc (bottom) skin sample, measured at (b) 1.9 ms, (c) 3.03 ms, (d) 3.67 ms, (e) 4.4 ms, and (f) 5 ms after excitation from an *in vivo* sample imaged at the center region. The white triangle represents the reference signal used in the velocity calculations, and the white arrow indicates the propagation of the elastic wave (Video 1, MPEG 1 MB) [URL: http://dx.doi.org/10.1117/1.JBO.21.4.046002.1].

Fig. 6. The Young's modulus of the healthy skin was 4.1 ± 1.9 kPa and was significantly less ($p < 0.05$) than the stiffness of the central region of the BLM-SSc affected skin, which was 36.6 ± 27.2 kPa.

Following BLM challenge, skin involvement demonstrates considerable spatial variation. Hence, we next tested if OCE could also capture less severe skin changes at the periphery of the affected skin lesions. The results depicted in Fig. 7 demonstrate that OCE was also able to distinguish the BLM-SSc affected skin at the periphery of the afflicted region from the healthy control skin ($p < 0.05$). The Young's moduli of the healthy and BLM-SSc skin, assessed *in vitro*, were 12.2 ± 7.1 and 52.6 ± 33.8 kPa, respectively, as plotted in Fig. 7(a). The *in vivo* elasticity assessments of the healthy skin and BLM-SSc skin at the periphery of the diseased region were 1.8 ± 0.7 and 5.2 ± 2.7 kPa, respectively. These values appear to be lower than the measurements recorded at the central regions of the affected skin (Fig. 6).

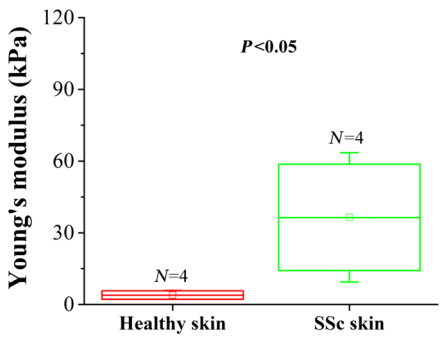

Fig. 6 *In vivo* OCE-assessment of skin involvement in the central regions of BLM-SSc-affected skin. Plotted are the Young's modulus of the healthy skin and the central region of the BLM-SSc-afflicted skin from the *in vivo* OCE measurements, assessed in four mice per study group.

4 Discussion

In this work, we have demonstrated the first use of noncontact OCE to detect elasticity differences between fibrotic and healthy murine skin samples, *in vitro* and *in vivo*, following BLM-induced SSc-like disease. The results show that this optical imaging method was able to successfully distinguish the fibrotic and healthy skin; importantly, fibrotic skin was significantly stiffer than the healthy skin. This correlates well with previous work using ultrasound elastography[39] and contact-based Vesmeter.[25] The increased Young's modulus and thickness observed in this study may be the direct consequence of increased collagen accumulation in SSc skin, which has been well documented in the SSc literature and reproduced by our histological analyses [Figs. 3(e)–3(g)]. In addition, the diseased samples showed a greater variance in elasticity as compared to the healthy skin. This may be due to differences in BLM-induced SSc progression between each individual sample and, consequently, collagen accumulation and distribution. The results from the OCE assessments at the margin of the

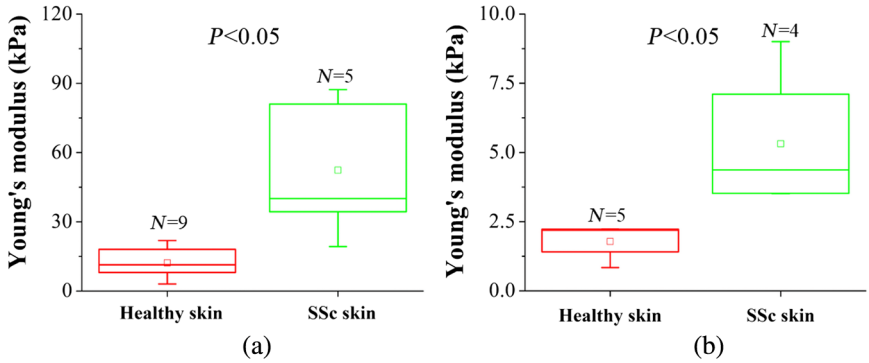

Fig. 7 *In vitro* and *in vivo* OCE assessment of skin involvement in the peripheral regions of BLM-SSc-affected skin. Plotted are the Young's modulus recorded in healthy skin and BLM-SSc-afflicted skin at the periphery of the diseased region, from (a) *in vitro* and (b) *in vivo* OCE measurements.

diseased region showed that this imaging technique has sufficient capability to detect less dramatic changes in elasticity in BLM-affected SSc skin, as plotted in Figs. 7(a) and 7(b). While it is difficult to assess gradations in the degree of skin thickening using the currently used mRSS metric, the OCE platform may offer accurate, graded assessment of skin involvement in SSc. Moreover, previous work has reported that the BLM-induced SSc model shows significant similarities with naturally developed SSc in patients,[40] which supports the clinical value of the presented results in this study.

Elasticity values quantified based solely on group wave velocity may not be entirely accurate. In addition, boundary conditions affect the elastic wave velocity. From Fig. 7, it can be seen that the stiffness of the *in vitro* samples, obtained after sacrificing the mice, was greater as compared to the *in vivo* samples. The *in vitro* skin samples were mounted on polystyrene foam during the imaging experiments, which may have introduced additional artifacts in stiffness measurements when compared to the skin during the *in vivo* measurements. We are currently investigating if these differences account for the differences in Young's modulus recorded *in vitro* versus *in vivo*. Regardless, the data demonstrate that PhS-SSOCE was able to detect and quantitate fibrotic and elastic changes in the skin that are typical of SSc.

For routine practical clinical application of noncontact OCE, further reduction in acquisition time may be required. In the present report, 501 M-mode images were acquired from each skin sample with 100 ms duration for each image. However, we have recently reported a noncontact phase-sensitive OCE technique at ~1.5 million A-lines per second where the elastic wave was directly imaged, resulting in a total acquisition time of ~30 ms.[41] In addition, only a single air-pulse was required for an elasticity assessment over a line, while in the presented work, an air-pulse was synchronized with each M-mode image. Moreover, due to the reduced data size, the computational cost for data processing can be significantly decreased. When coupled with GPU accelerated OCE,[42] this technique may be able to provide near-real-time elasticity estimates. Miniaturization of the components shown in Fig. 1 will allow this platform to be more practitioner-friendly in an outpatient clinic setting. Similar studies are clearly warranted in SSc patients to evaluate if OCE can be used to monitor skin involvement in SSc in a longitudinal fashion.

However, the measured elasticity by the proposed technique can be affected by sample conditions, such as thickness and curvature.[43] Hair on the skin can significantly hinder the propagation of the elastic wave, and differences in skin geometry may decrease the accuracy of the elasticity estimation. Thus, a flat hair-free portion of the skin would be required for accurate *in vivo* OCE assessment. For *in vitro* elasticity characterization, the sample thickness and boundary conditions during the OCE measurement can also affect the measured elasticity. Although the elastic wave velocity can be affected by the sample condition (e.g., geometry), OCE allows for a more sensitive and objective quantification as compared to the mRSS method.

5 Conclusion

To summarize, we have demonstrated the first use of noncontact OCE to identify elasticity changes in murine skin afflicted with BLM-induced SSc. The OCE and histopathological results were in good agreement, demonstrating the feasibility of OCE for detecting skin changes associated with SSc, even when the disease is mild. Due to its noncontact detection and loading, objective assessment, high spatial resolution, and ability to accurately detect SSc even at the periphery of the diseased region, OCE is a promising technique for SSc diagnosis and monitoring.

Acknowledgments

The authors are grateful to Mr. Chen Wu and Ms. Rasksha Raghunathan for experimental assistance, and to Dr. Zhaolong Han for the discussion of biomechanical skin properties. This work was supported in part by NIH R01 DK81872 (C.M.) and R01 EY022362, R01 HL120140, R01 HD086765, and U54 HG006348 (K.L.). The authors do not have any financial conflict of interest with respect to this study.

References

1. G. Abignano et al., "Virtual skin biopsy by optical coherence tomography: the first quantitative imaging biomarker for scleroderma," *Ann. Rheum. Dis.* **72**(11), 1845–1851 (2013).
2. A. Gabrielli, E. V. Avvedimento, and T. Krieg, "Scleroderma," *N. Engl. J. Med.* **360**(19), 1989–2003 (2009).
3. M. D. Mayes et al., "Prevalence, incidence, survival, and disease characteristics of systemic sclerosis in a large US population," *Arthritis Rheum.* **48**(8), 2246–2255 (2003).
4. C. P. Denton, "Advances in pathogenesis and treatment of systemic sclerosis," *Clin. Med.* **15**(Suppl 6), s58–s63 (2015).
5. C. P. Denton, "Systemic sclerosis: from pathogenesis to targeted therapy," *Clin. Exp. Rheumatol.* **33**(4 Suppl 92), S3–S7 (2015).
6. V. D. Steen and T. A. Medsger, "Changes in causes of death in systemic sclerosis, 1972–2002," *Ann. Rheum. Dis.* **66**(7), 940–944 (2007).

7. S. Amjadi et al., "Course of the modified Rodnan skin thickness score in systemic sclerosis clinical trials: analysis of three large multicenter, double-blind, randomized controlled trials," *Arthritis Rheum.* **60**(8), 2490–2498 (2009).
8. P. Clements et al., "Inter and intraobserver variability of total skin thickness score (modified Rodnan TSS) in systemic sclerosis," *J. Rheumatol.* **22**(7), 1281–1285 (1995).
9. L. Czirjak, I. Foeldvari, and U. Muller-Ladner, "Skin involvement in systemic sclerosis," *Rheumatology* **47**(Suppl 5), v44–v45 (2008).
10. R. Hesselstrand et al., "High-frequency ultrasound of skin involvement in systemic sclerosis reflects oedema, extension and severity in early disease," *Rheumatology* **47**(1), 84–87 (2008).
11. S. V. Castro and S. A. Jimenez, "Biomarkers in systemic sclerosis," *Biomarkers Med.* **4**(1), 133–147 (2010).
12. A. Pagnoni et al., "Optical coherence tomography in dermatology," *Skin Res. Technol.* **5**(2), 83–87 (1999).
13. O. Babalola et al., "Optical coherence tomography (OCT) of collagen in normal skin and skin fibrosis," *Arch. Dermatol. Res.* **306**(1), 1–9 (2014).
14. J. L. Tedstone et al., "Ultrasound imaging accurately detects skin thickening in a mouse scleroderma model," *Ultrasound Med. Biol.* **34**(8), 1239–1247 (2008).
15. M. Crisan et al., "Ultrasonographic staging of cutaneous malignant tumors: an ultrasonographic depth index," *Arch. Dermatol. Res.* **305**(4), 305–313 (2013).
16. Y. P. Huang et al., "High frequency ultrasound assessment of skin fibrosis: clinical results," *Ultrasound Med. Biol.* **33**(8), 1191–1198 (2007).
17. D. Huang et al., "Optical coherence tomography," *Science* **254**(5035), 1178–1181 (1991).
18. T. Gambichler, V. Jaedicke, and S. Terras, "Optical coherence tomography in dermatology: technical and clinical aspects," *Arch. Dermatol. Res.* **303**(7), 457–473 (2011).
19. M. C. Pierce et al., "Advances in optical coherence tomography imaging for dermatology," *J. Invest. Dermatol.* **123**(3), 458–463 (2004).
20. M. C. Pierce et al., "Collagen denaturation can be quantified in burned human skin using polarization-sensitive optical coherence tomography," *Burns* **30**(6), 511–517 (2004).
21. V. R. Korde et al., "Using optical coherence tomography to evaluate skin sun damage and precancer," *Laser Surg. Med.* **39**(9), 687–695 (2007).
22. S. Wang et al., "Three-dimensional computational analysis of optical coherence tomography images for the detection of soft tissue sarcomas," *J. Biomed. Opt.* **19**(2), 021102 (2014).
23. A. Balbir-Gurman et al., "Non-invasive measurement of biomechanical skin properties in systemic sclerosis," *Ann. Rheum. Dis.* **61**(3), 237–241 (2002).
24. V. Falanga and B. Bucalo, "Use of a durometer to assess skin hardness," *J. Am. Acad. Dermatol.* **29**(1), 47–51 (1993).
25. Y. Kuwahara et al., "Quantification of hardness, elasticity and viscosity of the skin of patients with systemic sclerosis using a novel sensing device (Vesmeter): a proposal for a new outcome measurement procedure," *Rheumatology* **47**(7), 1018–1024 (2008).
26. J. Schmitt, "OCT elastography: imaging microscopic deformation and strain of tissue," *Opt. Express* **3**(6), 199 (1998).
27. S. Wang and K. V. Larin, "Optical coherence elastography for tissue characterization: a review," *J. Biophotonics* **8**(4), 279–302 (2015).
28. R. K. Manapuram, V. G. R. Manne, and K. V. Larin, "Phase-sensitive swept source optical coherence tomography for imaging and quantifying of microbubbles in clear and scattering media," *J. Appl. Phys.* **105**(10), 102040 (2009).
29. R. K. Manapuram, V. G. R. Manne, and K. V. Larin, "Development of phase-stabilized swept-source OCT for the ultrasensitive quantification of microbubbles," *Laser Phys.* **18**(9), 1080–1086 (2008).
30. S. Wang et al., "A focused air-pulse system for optical-coherence-tomography-based measurements of tissue elasticity," *Laser Phys. Lett.* **10**(7), 075605 (2013).
31. S. Wang and K. V. Larin, "Shear wave imaging optical coherence tomography (SWI-OCT) for ocular tissue biomechanics," *Opt. Lett.* **39**(1), 41–44 (2014).
32. R. K. Manapuram et al., "Estimation of shear wave velocity in gelatin phantoms utilizing PhS-SSOCT," *Laser Phys.* **22**(9), 1439–1444 (2012).
33. S. Song, Z. Huang, and R. K. Wang, "Tracking mechanical wave propagation within tissue using phase-sensitive optical coherence tomography: motion artifact and its compensation," *J. Biomed. Opt.* **18**(12), 121505 (2013).
34. O. Vargas et al., "Use of an agent to reduce scattering in skin," *Laser Surg. Med.* **24**(2), 133–141 (1999).
35. S. Wang et al., "Noncontact quantitative biomechanical characterization of cardiac muscle using shear wave imaging optical coherence tomography," *Biomed. Opt. Express* **5**(7), 1980–1992 (2014).
36. S. J. Kirkpatrick, D. D. Duncan, and L. Fang, "Low-frequency surface wave propagation and the viscoelastic behavior of porcine skin," *J. Biomed. Opt.* **9**(6), 1311–1319 (2004).
37. Z. Han et al., "Quantitative methods for reconstructing tissue biomechanical properties in optical coherence elastography: a comparison study," *Phys. Med. Biol.* **60**(9), 3531–3547 (2015).
38. Y. Wang et al., "Compressive viscoelasticity of freshly excised mouse skin is dependent on specimen thickness, strain level and rate," *PLoS One* **10**(3), e0120897 (2015).
39. A. Iagnocco et al., "Ultrasound elastography assessment of skin involvement in systemic sclerosis: lights and shadows," *J. Rheumatol.* **37**(8), 1688–1691 (2010).
40. I. Y. Adamson and D. H. Bowden, "The pathogenesis of bleomycin-induced pulmonary fibrosis in mice," *Am. J. Pathol.* **77**(2), 185–197 (1974).
41. M. Singh et al., "Phase-sensitive optical coherence elastography at 1.5 million A-lines per second," *Opt. Lett.* **40**(11), 2588–2591 (2015).
42. R. Kirk et al., "Near video-rate optical coherence elastography by acceleration with a graphics processing unit," *J. Lightwave Technol.* **33**(16), 3481–3485 (2015).
43. Z. Han et al., "Analysis of the effects of curvature and thickness on elastic wave velocity in cornea-like structures by finite element modeling and optical coherence elastography," *Appl. Phys. Lett.* **106**(23), 233702 (2015).

Yong Du is research assistant professor of biomedical engineering of University of Houston. He received his PhD in internal medicine/nephrology from Sun Yat-sen University, China, in 2004. He completed his postdoctoral training in internal medicine/rheumatology at UT Southwestern Medical Center. He has authored over 30 peer-reviewed papers, reviews, and book chapters. His work focuses on the cellular and molecular pathogenesis of lupus nephritis.

Chih-Hao Liu received his BS degree in electrical engineering from National Taiwan University of Science and Technology (2010), and his MS degree in biomedical engineering from National Taiwan University (2013). He is currently a PhD candidate in the Department of Biomedical Engineering at the University of Houston. His research interests focus on system development of optical coherence tomography (elastography), automated fringe analysis, and tissue biomechanics.

Ling Lei is a rheumatology physician of the First Affiliated Hospital of Guangxi Medical University in China. She received her PhD in Guangxi Medical University, China, in 2012. As a rheumatology physician, she mastered the basic skills and knowledge of autoimmune disease and the pathogenesis of systemic sclerosis (SSc). She has been a visiting scholar starting from 2014 to 2015 in the Department of Biomedical Engineering at the University of Houston. She has contributed to more than 20 peer-reviewed articles, with 10 as the first author.

Manmohan Singh received his BS degree in biomedical engineering from the University of Houston in 2014. He is currently pursuing his PhD in the Department of Biomedical Engineering at the University of Houston. Since the fall of 2010, he has been with Dr. Kirill Larin's Biomedical Optics Laboratory. His research interests include utilizing biomedical imaging for the detection of diseases and utilizing and developing new elastographic methods for investigating the biomechanical properties of tissues.

Jiasong Li received his BS degree in biomedical engineering from Northeastern University, Shenyang, Liaoning, China, in 2007. He became a graduate student at Huazhong University of Science and Technology, Wuhan, Hubei, China, in 2008. He is currently a PhD candidate in the Department of Biomedical Engineering at the University of Houston. His current research is focused on

development and applications of optical coherence tomography (elastography) systems.

M. John Hicks MD, DDS, MS, PhD, is board certified in anatomic and pediatric pathology and professor of pathology, pediatrics, and immunology at Baylor College of Medicine and adjunct professor at the University of Texas School of Dentistry in Houston. He is an attending pediatric pathologist in the Department of Pathology at Baylor College of Medicine in Houston Texas. He has published over 400 peer-review manuscripts and 30 chapters. He participates in collaborative research in the areas of autoimmune disease, medical renal disease, and pediatric malignancies.

Kirill V. Larin is a professor of biomedical engineering at the University of Houston. He received his MS degree in laser physics and mathematics from Saratov State University (1995) and his PhD in biomedical engineering from the University of Texas Medical Branch in Galveston (2002). He has published more than 100 papers in the field of biomedical optics and biophotonics. He is a fellow of SPIE (2015) and OSA (2016).

Chandra Mohan currently holds the Cullen Distinguished Professorship at the University of Houston, in Houston, Texas. He is an elected member of the American Society of Clinical Investigation and the Henry Kunkel Society. He undertook his doctoral thesis work focusing on the cellular immunology of lupus at Tufts University. Currently, his laboratory's research efforts have concentrated on elucidating the cellular, molecular, and genetic players leading to murine lupus, with corresponding translational studies in human lupus.